



HAL
open science

Revisiting short-wave-infrared (SWIR) bands for atmospheric correction in coastal waters

Nima Pahlevan, Jean-Claude Roger, Ziauddin Ahmad

► **To cite this version:**

Nima Pahlevan, Jean-Claude Roger, Ziauddin Ahmad. Revisiting short-wave-infrared (SWIR) bands for atmospheric correction in coastal waters. *Optics Express*, 2017, 25 (6), pp.6015. 10.1364/OE.25.006015 . hal-03469877

HAL Id: hal-03469877

<https://uca.hal.science/hal-03469877>

Submitted on 21 Dec 2023

HAL is a multi-disciplinary open access archive for the deposit and dissemination of scientific research documents, whether they are published or not. The documents may come from teaching and research institutions in France or abroad, or from public or private research centers.

L'archive ouverte pluridisciplinaire **HAL**, est destinée au dépôt et à la diffusion de documents scientifiques de niveau recherche, publiés ou non, émanant des établissements d'enseignement et de recherche français ou étrangers, des laboratoires publics ou privés.



Distributed under a Creative Commons Attribution 4.0 International License

Revisiting short-wave-infrared (SWIR) bands for atmospheric correction in coastal waters

NIMA PAHLEVAN,^{1,2,*} JEAN-CLAUDE ROGER,^{1,3} AND ZIAUDDIN AHMAD^{1,4}

¹NASA Goddard Space Flight Center, 8800 Greenbelt Rd. Greenbelt MD 20771, USA

²Science Systems and Applications, 10210 Greenbelt Road, Lanham MD 20706, USA

³Department of Geographical Sciences, University of Maryland College Park 20740, USA

⁴JHT, Inc., 2001 Jefferson Davis Hwy # 309, Arlington, VA 22202, USA

*nima.pahlevan@nasa.gov

Abstract: The shortwave infrared (SWIR) bands on the existing Earth Observing missions like MODIS have been designed to meet land and atmospheric science requirements. The future geostationary and polar-orbiting ocean color missions, however, require highly sensitive SWIR bands ($> 1550\text{nm}$) to allow for a precise removal of aerosol contributions. This will allow for reasonable retrievals of the remote sensing reflectance (R_{rs}) using standard NASA atmospheric corrections over turbid coastal waters. Design, fabrication, and maintaining high-performance SWIR bands at very low signal levels bear significant costs on dedicated ocean color missions. This study aims at providing a full analysis of the utility of alternative SWIR bands within the 1600nm atmospheric window if the bands within the 2200nm window were to be excluded due to engineering/cost constraints. Following a series of sensitivity analyses for various spectral band configurations as a function of water vapor amount, we chose spectral bands centered at 1565 and 1675nm as suitable alternative bands within the 1600nm window for a future geostationary imager. The sensitivity of this band combination to different aerosol conditions, calibration uncertainties, and extreme water turbidity were studied and compared with that of all band combinations available on existing polar-orbiting missions. The combination of the alternative channels was shown to be as sensitive to test aerosol models as existing near-infrared (NIR) band combinations (e.g., 748 and 869nm) over clear open ocean waters. It was further demonstrated that while in extremely turbid waters the 1565/1675 band pair yields R_{rs} retrievals as good as those derived from all other existing SWIR band pairs ($> 1550\text{nm}$), their total calibration uncertainties must be $< 1\%$ to meet current science requirements for ocean color retrievals (i.e., $\Delta R_{rs} (443) < 5\%$). We further show that the aerosol removal using the NIR and SWIR bands (available on the existing polar-orbiting missions) can be very sensitive to calibration uncertainties. This requires the need for monitoring the calibration of these bands to ensure consistent multi-mission ocean color products in coastal/inland waters.

© 2017 Optical Society of America

OCIS codes: (010.0280) Remote sensing and sensors; (010.1285) Atmospheric correction.

References and links

1. H. R. Gordon, "Radiative transfer: a technique for simulating the ocean in satellite remote sensing calculations," *Appl. Opt.* **15**(8), 1974–1979 (1976).
2. H. R. Gordon and M. Wang, "Retrieval of water-leaving radiance and aerosol optical thickness over the oceans with SeaWiFS: a preliminary algorithm," *Appl. Opt.* **33**(3), 443–452 (1994).
3. H. R. Gordon, "Removal of atmospheric effects from satellite imagery of the oceans," *Appl. Opt.* **17**(10), 1631–1636 (1978).
4. C. D. Mobley, J. Werdell, B. Franz, Z. Ahmad, and S. Bailey, "Atmospheric correction for satellite ocean color radiometry," Tech Rep. (2016).
5. M. Wang, "Atmospheric correction for remotely-sensed ocean-colour products," Reports and Monographs of the International Ocean-Colour Coordinating Group (IOCCG) (2010).
6. H. R. Gordon and D. J. Castaño, "Coastal Zone Color Scanner atmospheric correction algorithm: multiple scattering effects," *Appl. Opt.* **26**(11), 2111–2122 (1987).
7. H. R. Gordon, J. W. Brown, and R. H. Evans, "Exact Rayleigh scattering calculations for use with the Nimbus-7 coastal zone color scanner," *Appl. Opt.* **27**(5), 862–871 (1988).

8. H. R. Gordon and M. Wang, "Surface-roughness considerations for atmospheric correction of ocean color sensors. I: The Rayleigh-scattering component," *Appl. Opt.* **31**(21), 4247–4260 (1992).
9. M. Wang, "Atmospheric correction of ocean color sensors: computing atmospheric diffuse transmittance," *Appl. Opt.* **38**, 451–455 (1999).
10. H. Yang and H. R. Gordon, "Remote sensing of ocean color: assessment of water-leaving radiance bidirectional effects on atmospheric diffuse transmittance," *Appl. Opt.* **36**(30), 7887–7897 (1997).
11. C. D. Mobley, *Light and Water: Radiative Transfer in Natural Waters* (Academic Press, Inc., 1994).
12. D. A. Siegel, M. Wang, S. Maritorena, and W. Robinson, "Atmospheric correction of satellite ocean color imagery: the black pixel assumption," *Appl. Opt.* **39**(21), 3582–3591 (2000).
13. A. R. A. Stumpf, R. P. Gould, Jr., P. M. Martinolich, and V. Ransibrahmanakul, "A partially coupled ocean-atmosphere model for retrieval of water-leaving radiance from SeaWiFS in coastal waters," (National Aeronautics and Space Administration, Goddard Space Flight Center, Greenbelt, MD, Patt, F.S., et al., 2003: Algorithm Updates for the Fourth SeaWiFS Data Reprocessing, 2004).
14. S. W. Bailey, B. A. Franz, and P. J. Werdell, "Estimation of near-infrared water-leaving reflectance for satellite ocean color data processing," *Opt. Express* **18**(7), 7521–7527 (2010).
15. K. G. Ruddick, F. Ovidio, and M. Rijkeboer, "Atmospheric correction of SeaWiFS imagery for turbid coastal and inland waters," *Appl. Opt.* **39**(6), 897–912 (2000).
16. B.-C. Gao, M. J. Montes, Z. Ahmad, and C. O. Davis, "Atmospheric correction algorithm for hyperspectral remote sensing of ocean color from space," *Appl. Opt.* **39**(6), 887–896 (2000).
17. M. Wang, "Remote sensing of the ocean contributions from ultraviolet to near-infrared using the shortwave infrared bands: simulations," *Appl. Opt.* **46**(9), 1535–1547 (2007).
18. W. Shi and M. Wang, "An assessment of the black ocean pixel assumption for MODIS SWIR bands," *Remote Sens. Environ.* **113**(8), 1587–1597 (2009).
19. M. Wang and W. Shi, "The NIR-SWIR combined atmospheric correction approach for MODIS ocean color data processing," *Opt. Express* **15**(24), 15722–15733 (2007).
20. P. J. Werdell, B. A. Franz, and S. W. Bailey, "Evaluation of shortwave infrared atmospheric correction for ocean color remote sensing of Chesapeake Bay," *Remote Sens. Environ.* **114**(10), 2238–2247 (2010).
21. M. Wang and W. Shi, "Sensor noise effects of the SWIR bands on MODIS-derived ocean color products," *IEEE Trans. Geosci. Remote Sens.* **50**(9), 3280–3292 (2012).
22. Q. Vanhellemont and K. Ruddick, "Advantages of high quality SWIR bands for ocean colour processing: Examples from Landsat-8," *Remote Sens. Environ.* **161**, 89–106 (2015).
23. B. A. Franz, S. W. Bailey, N. Kuring, and P. J. Werdell, "Ocean color measurements with the Operational Land Imager on Landsat-8: implementation and evaluation in SeaDAS," *J. Appl. Remote Sens.* **9**(1), 096070 (2015).
24. N. Pahlevan, J. R. Schott, B. A. Franz, G. Zibordi, B. Markham, S. Bailey, C. B. Schaaf, M. Ondrusek, S. Greb, and C. M. Strait, "Landsat 8 remote sensing reflectance (R_{rs}) products: Evaluations, intercomparisons, and enhancements," *Remote Sens. Environ.* **190**, 289–301 (2017).
25. G. Zibordi, F. Mélin, J.-F. Berthon, B. Holben, I. Slutsker, D. Giles, D. D'Alimonte, D. Vandemark, H. Feng, G. Schuster, B. E. Fabbri, S. Kaitala, and J. Seppälä, "AERONET-OC: A Network for the Validation of Ocean Color Primary Products," *J. Atmos. Ocean. Technol.* **26**(8), 1634–1651 (2009).
26. C. Del Castillo, S. Platnick, and D. Antoine, "Pre-Aerosol, Clouds, and ocean Ecosystem (PACE) Mission Science Definition Team Report," (NASA Goddard Space Flight Center, 2012).
27. J. I. Fishman, L. T. Al-Saadi, J. Chance, K. Chavez, F. Chin, M. Coble, P. Davis, C. DiGiacomo, P. M. Edwards, D. Elderling, A. Goes, J. Herman, J. Hu, C. Jacob, D. J. Jordan, C. Kawa, S. R. Key, R. Liu, X. Lohrenz, S. Mannino, A. Natraj, V. Neil, D. Neu, J. Newchurch, M. Pickering, K. Salisbury, J. Sosik, H. Subramaniam, A. Tzortziou, M. Wang, and J. Wang, "The United States' Next Generation of Atmospheric Composition and Coastal Ecosystem Measurements: NASA's Geostationary Coastal and Air Pollution Events (GEO-CAPE) Mission," *Bull. Am. Meteorol. Soc.* **93**, 19 (2012).
28. C. Hu, L. Feng, Z. Lee, C. O. Davis, A. Mannino, C. R. McClain, and B. A. Franz, "Dynamic range and sensitivity requirements of satellite ocean color sensors: learning from the past," *Appl. Opt.* **51**(25), 6045–6062 (2012).
29. M. Wang, W. Shi, L. Jiang, and K. Voss, "NIR- and SWIR-based on-orbit vicarious calibrations for satellite ocean color sensors," *Opt. Express* **24**(18), 20437–20453 (2016).
30. R. Showstack, "Sentinel satellites initiate new era in earth observation," *Eos (Wash. D.C.)* **95**(26), 239–240 (2014).
31. M. Wang and S. W. Bailey, "Correction of Sun glint Contamination on the SeaWiFS Ocean and Atmosphere Products," *Appl. Opt.* **40**(27), 4790–4798 (2001).
32. Z. Ahmad, B. A. Franz, C. R. McClain, E. J. Kwiatkowska, J. Werdell, E. P. Shettle, and B. N. Holben, "New aerosol models for the retrieval of aerosol optical thickness and normalized water-leaving radiances from the SeaWiFS and MODIS sensors over coastal regions and open oceans," *Appl. Opt.* **49**(29), 5545–5560 (2010).
33. H. R. Gordon, "Atmospheric correction of ocean color imagery in the Earth Observing System era," *J. Geophys. Res. Atmos.* **102**(D14), 17081–17106 (1997).
34. B. N. Holben, T. F. Eck, I. Slutsker, D. Tanré, J. P. Buis, A. Setzer, E. Vermote, J. A. Reagan, Y. J. Kaufman, T. Nakajima, F. Lavenue, I. Jankowiak, and A. Smirnov, "AERONET—A Federated Instrument Network and Data Archive for Aerosol Characterization," *Remote Sens. Environ.* **66**(1), 1–16 (1998).

35. O. Dubovik, B. Holben, T. F. Eck, A. Smirnov, Y. J. Kaufman, M. D. King, D. Tanré, and I. Slutsker, "Variability of absorption and optical properties of key aerosol types observed in worldwide locations," *J. Atmos. Sci.* **59**(3), 590–608 (2002).
36. M. Wang and H. R. Gordon, "Calibration of ocean color scanners: how much error is acceptable in the near infrared?" *Remote Sens. Environ.* **82**(2-3), 497–504 (2002).
37. B. A. Franz, S. W. Bailey, P. J. Werdell, and C. R. McClain, "Sensor-independent approach to the vicarious calibration of satellite ocean color radiometry," *Appl. Opt.* **46**(22), 5068–5082 (2007).
38. W. L. Barnes, T. S. Pagano, and V. V. Salomonson, "Prelaunch characteristics of the moderate resolution imaging spectroradiometer (MODIS) on EOS-AM1," *IEEE Trans. Geosci. Remote Sens.* **36**(4), 1088–1100 (1998).
39. E. Knaeps, K. Ruddick, D. Doxaran, A. Dogliotti, B. Nechad, D. Raymaekers, and S. Sterckx, "A SWIR based algorithm to retrieve total suspended matter in extremely turbid waters," *Remote Sens. Environ.* **168**, 66–79 (2015).
40. P. D. Kunte, "Sediment concentration and bed form structures of Gulf of Cambay from remote sensing," *Int. J. Remote Sens.* **29**(8), 2169–2182 (2008).
41. Z. Lee, S. Shang, G. Lin, J. Chen, and D. Doxaran, "On the modeling of hyperspectral remote-sensing reflectance of high-sediment-load waters in the visible to shortwave-infrared domain," *Appl. Opt.* **55**(7), 1738–1750 (2016).

1. Introduction

During the early ocean color era, prior to the launch of the coastal zone color scanner (CZCS), the radiative transfer analyses had shown that most of the "blue" photons reaching top of atmosphere (TOA) over seawaters arise from the atmospheric column [1,2]. The impact of atmosphere is through scattering and absorption processes induced by the molecules, aerosols, and gases. Gordon [1] further evaluated the sensitivity required to detect small changes in TOA radiances to enable detecting changes in water-leaving radiances. Using the single scattering approximations (assuming no scattering between the molecules and aerosols), Gordon [3] proposed to use the band ratios of two channels within the red and near infrared (NIR) portion of the spectrum (where the upwelling radiance field can be assumed negligible over open ocean) to infer the aerosol contribution to the TOA signal. This was proposed under the assumption that the Rayleigh scattering contributions can be sufficiently accurately computed and subtracted from the TOA signal. This work laid out the basis for the current operational algorithm utilized by the NASA Ocean Biology Processing Group (OBPG) [4]. Over the past years, however, the band-ratio aerosol determinations and other components of the atmospheric correction (AC) process were enhanced [5]. This is comprised of using two dedicated NIR bands and a vector radiative transfer code [6,7], correcting for Rayleigh-aerosol interactions [2], accounting for wind-induced sea surface variations [8], and accurate calculations of diffuse sensor-surface transmittance [8–10]. The algorithm has been shown to provide sufficiently accurate remote sensing reflectance R_{rs} , defined as the ratio of water-leaving radiance and downwelling irradiance just above the surface) over oceanic waters [11]. The determination of the band ratio value (ϵ), however, in the presence of non-zero water-leaving radiances within the NIR portion of the spectrum was found to overestimate aerosol contributions leading to underestimating the R_{rs} spectrum [12]. One way to surmount this misinterpretation of the aerosol signal is to use bio-optical models to estimate the NIR water-leaving radiance [13,14]. This is carried out through an iterative process to remove the water-leaving signal from the Rayleigh-corrected signal. At regional scales, knowing the relationship between the red and NIR water-leaving radiances, one can also account for the NIR upwelling signal and improve R_{rs} retrievals [15]. The other method is to utilize SWIR bands where R_{rs} can be assumed zero [16]. This technique uses a spectral matching method using the shortwave infrared SWIR channels of the Airborne Visible/Infrared Imaging Spectrometer (AVIRIS). Wang [17] extended the Gordon and Wang [2] (GW94) algorithm to the SWIR bands onboard the Moderate Resolution Imaging Spectroradiometer (MODIS) for AC over coastal turbid waters. The algorithm, which was based upon the same rational as in the earlier research work [2], was implemented and tested

for various extremely turbid waters [18,19]. However, the major drawback of the use of MODIS channels is their relatively low signal-to-noise ratios (SNRs) over bodies of water, which results in noisy retrievals [20,21] when compared to retrievals through the iterative NIR method [14]. Very recently, the SWIR bands of the Operational Land Imager (OLI) aboard Landsat-8 have successfully been used for atmospheric correction (AC) over coastal waters [22,23]. The performance has shown promising results [24] through extensive comparisons against standard ocean color R_{rs} products and validations at the ocean color component of the Aerosol Robotic Network (AERONET) [25].

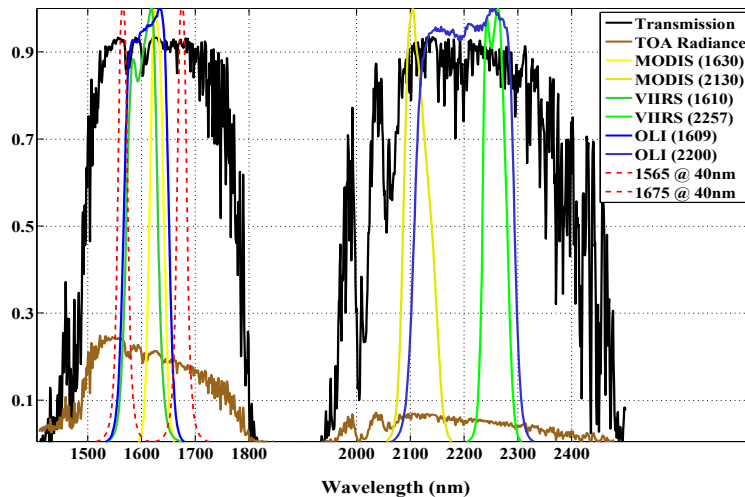


Fig. 1. The relative spectral response (RSR) functions overlaid on an atmospheric transmission curve and TOA radiance spectrum ($\text{wm}^{-2}\text{sr}^{-1}\mu^{-1}$) shown for the two 1600nm and 2200nm atmospheric windows. The spectral responses (unitless) shown are those of MODIS, VIIRS, and OLI as well as two narrow ones (@20nm) towards the sides of the 1600nm window.

Although incorporating the SWIR bands for future NASA ocean color missions have been recommended [26,27], the addition of the SWIR bands bears additional costs and adds complexities in the overall instrument design (e.g., SWIR detectors require radiators to maintain high performance). The SWIR spectral bands are commonly designed within the atmospheric windows where reflected solar spectra reach top of atmosphere. These include 1240nm, 1600nm, and 2200nm, SWIR windows. While placements, bandwidths, and the SNR requirements of the SWIR bands designed for missions like MODIS were targeted for scientific applications for clouds, aerosol, land, and fire, future NASA ocean color missions may be equipped with SWIR bands whose radiometric sensitivities are higher [26,28]. The SWIR bands commonly used and examined for AC are the ones available on MODIS, i.e., 1240nm, 1630nm, and 2130nm. Although the Visible Infrared Imaging Radiometer Suite (VIIRS) aboard Suomi NPP is also equipped with SWIR bands, there has been no attempt (operationally) to utilize its SWIR bands for AC. Only recently, its calibration has been vicariously updated for use [29]. Figure 1 illustrates the 1600nm and 2200nm atmospheric transmission windows (solid black curves) with the MODIS, VIIRS, and OLI relative spectral response (RSR) functions overlaid. Further details on the RSRs are tabulated in Table 1. The two narrow, dashed response curves drawn towards the shoulders of the 1600nm window will be discussed in the following sections. Note that an average TOA radiance spectrum ($\text{wm}^{-2}\text{sr}^{-1}\mu^{-1}$) over bodies of water for near-nadir viewing geometry is also shown.

Table 1. The specifications of the SWIR bands of MODIS, VIIRS, and OLI SWIR studied here.

	OLI	VIIRS	MODIS	MODIS	OLI	VIIRS
Band Center (nm)	1609	1610	1630	2130	2200	2257
Bandwidth (nm)	80	60	24	50	180	50

In addition to NASA missions with ocean color capability, the European Space Agency (ESA) has planned a constellation of satellite missions with similar capabilities [30]. These include the MultiSpectral Imager (MSI) and the Sea and Land Surface Temperature Radiometer (SLSTR), which are both capable of making measurements in the SWIR region. The SWIR bands of MSI and SLSTR are very similar to those of OLI and VIIRS. More specifically, within the 1600nm window, the OLI (1609nm), MSI (1610nm), and SLSTR (1610nm) bands have near-identical bandwidths with slight differences in the peak of the response. Similarly, the 2200nm bands of OLI (2200nm) and MSI (2190nm) as well as those of VIIRS (2257nm) and SLSTR (2250nm) are similar in both bandwidths and shapes. Due to all the similarities, we suffice by referring only to the band centers of OLI and VIIRS throughout this manuscript.

Overall, the design challenges and the costs associated with the SWIR bands may increase towards longer wavelengths. One reason is the demand for maintaining lower operating temperatures of the detectors within the 2200nm window. It is thus critical to evaluate how strictly the success of AC in coastal/inland waters depends on the bands in the 2200nm window and whether alternative channels in the 1600nm window can be proposed to reduce future mission risks.

To this end, this manuscript aims at evaluating the suitability of alternative SWIR bands placed within the 1600nm window, i.e., 1565, 1610, and 1675nm, for the atmospheric correction (AC) utilizing the GW94 algorithm [2]. The performance of the AC using the combinations of these alternative channels is compared against the combination of existing channels available on MODIS, VIIRS, OLI, MSI, and SLSTR. Therefore, the results are applicable to the existing missions for intercomparisons of the performance. For completeness, the performance is also assessed when a new set of channels within the 2200nm window is employed. We will first evaluate the sensitivity of various band centers and bandwidths to water vapor absorption and choose optimal band placements. Then, these alternative bands will undergo testing for their sensitivity to a) various aerosol models/conditions, b) radiometric calibration uncertainties, and c) non-negligible water-leaving radiances in extremely turbid waters. The manuscript, therefore, follows by describing the selection of alternative bands (Section 2) and the implementations and analyses of the AC in Section 3. Sections 4 and 5 address the sensitivity of band combinations to calibration uncertainties and to extreme upper-water-column turbidity. The future directions and recommendations are discussed in the conclusions.

2. Water vapor absorption and band selection

For a dedicated ocean color mission, the primary factors influencing the selection of alternative bands within the SWIR region are their sensitivity to water vapor (WV) absorptions and their feasibility of maintaining high radiometric performances. While the latter is beyond the scope of this manuscript, simulations were conducted to assess the suitability of various band centers and bandwidths within the 1600 and 2200nm windows. As shown in Fig. 1, the 1600nm and 2200nm windows approximately provide ~ 200nm-wide regions to measure reflected solar energy. To begin with the simulations, the Lorentzian function was chosen to represent the relative spectral responses (RSR) for a combination of various band centers (i) and bandwidths (j). Following several experiments, we found the Lorentzian function to be more representative of a filter function than a single Gaussian

function. Two examples of these functions are shown in Fig. 1 (dashed, red curves). The Lorentzian function is written as below

$$\text{RSR}(i) = \frac{1}{1 + \left(\frac{2|\lambda - i|}{\text{FWHM}} \right)^\kappa} \quad (1)$$

where λ is the wavelength varying within the range of 1500 nm and 2400 nm with increments of 0.001 nm and κ is a variable that controls the shape of the RSRs. κ is a variable that controls the shape of the RSRs. The band centers (i) vary with increments of 5 nm. The full-width half maximum (FWHM), i.e., 50% of the maximum response, was chosen to be at 20, 40, 60, and 80 nm to simulate various bandwidths. We also chose $\kappa = 3.3$ for all the analyses to make the width at 1% of the maximum response 4X wider than that at the 50% response. This allows for incorporating some out-of-band response into the total integrated response. To evaluate the sensitivity to different total water vapor amounts, the MODerate resolution atmospheric TRANsmission code (MODTRAN) was utilized.

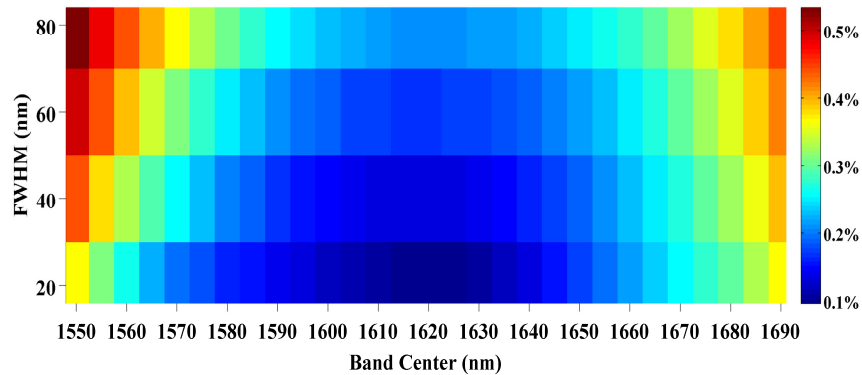


Fig. 2. The % error in TOA radiance as a result of 6% error in water vapor (WV) estimation provided for different band centers and bandwidths (FWHM) within the 1600nm window. With the increase in the bandwidths towards the edges, the water vapor contamination increases. The 20-nm bands centered at 1565 and 1675nm exhibit as much contamination as for a 80-nm band centered at 1620 nm (where the impact of WV absorption is minimal).

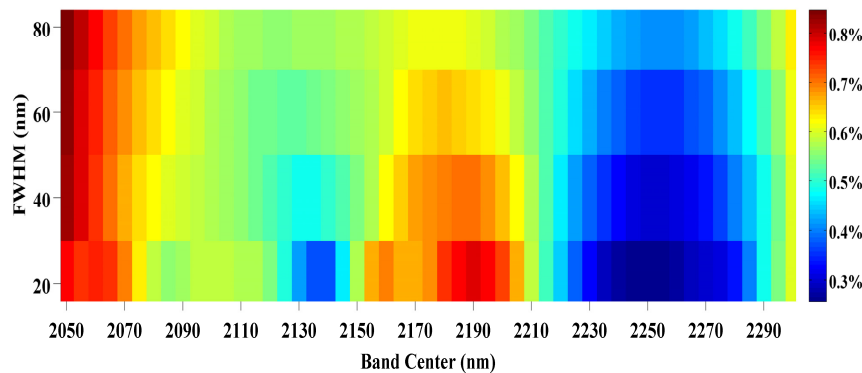


Fig. 3. The % error in TOA radiance as a result of 6% error in water vapor (WV) estimation given for different band centers and bandwidths (FWHM) within the 2200nm window. With the increase in the bandwidths towards the shorter wavelengths, the water vapor contamination increases. An optimal band should be placed in the vicinity of the 2260nm.

The WV amount was then scaled by $\pm 2\%$, $\pm 4\%$, and $\pm 6\%$ (δWV) to infer corresponding impacts on TOA radiance predications. The simulations were performed for viewing zenith angles (VZA) of 0° and 60° and solar zenith angles (SZA) of 30° and 60° . To capture all the spectral features, high-resolution band models and spectral grids were applied. The WV amount was then scaled by $\pm 2\%$, $\pm 4\%$, and $\pm 6\%$ (δWV) to infer corresponding impacts on TOA radiance predications. The simulations were performed for viewing zenith angles (VZA) of 0° and 60° and solar zenith angles (SZA) of 30° and 60° . To capture all the spectral features, high-resolution band models and spectral grids were applied.

The results of the sensitivity analysis is illustrated in the form of a sensitivity map in Fig. 2. It illustrates the % errors in TOA radiance associated with each band center and FWHM as a result of 6% error in estimating water vapor (i.e., $\delta WV = 6\%$). This is given for the largest air mass fractions, i.e., $VZA = SZA = 60^\circ$ representing the maximum expected impact on TOA observations. It is clearly seen that towards the center of the band pass (~ 1610 - 1620 nm) and $FWHM=20$ nm, there is minimal impact (i.e., $< 0.2\%$) due to WV absorption on predicting TOA radiances. This band specification could potentially be the optimal band setting for an ocean color mission. However, high SNR requirements can make the design of such a narrow band a challenging task. Thus, the bandwidth can be broadened up to 80 nm, which leads to $\sim 0.4\%$ error within the 1610-1640nm range for large air mass fractions. In fact, the OLI's (or MSI's) SWIR band is placed at 1610 nm with $FWHM=80$ nm (Table 1). The analysis for the near-nadir geometry (not show here) revealed $\sim 0.35\%$ error for the same band setting. Note that while the % error linearly increases with the increase of FWHM, the error abruptly rises for $FWHM=100$ nm as the absorption features begin to significantly influence the TOA radiance.

In general, relatively large bandwidths are desired for the SWIR bands onboard polar orbiting missions. The larger bandwidths allow for collecting more photons in a very short amount of time. However, for an imaging system onboard a geostationary platform where longer integration times are feasible, it is possible to design narrow bands (e.g., 20-nm) towards the edges of this window, i.e., 1565 and 1675nm, while maintaining high radiometric performances (Fig. 1). These band configurations carry $< 0.4\%$ error induced by a 6% error in WV estimation (similar to a ~ 1620 nm with $FWHM=80$ nm). In Section 3, we will further evaluate the utility of these two narrow bands for the aerosol removal and compare with the performances of bands onboard polar orbiting missions. Note also that further analysis of the simulation results indicated linear variations in TOA radiance relative to changes in δWV (not shown here). The slopes of variations were found different for different bands given the impact of WV absorption.

For completeness, a similar analysis (for an identical imaging geometry and an error level) is presented for the 2200nm window (Fig. 3). First, the spectral map indicates a larger sensitivity to WV absorption when compared to that shown in Fig. 2. Second, it is inferred that the 2240-2260 nm range exhibits a minimal sensitivity ($\sim 0.4\%$) to the WV absorption. This is, in fact, where one of the VIIRS (or SLSTR) SWIR bands is situated (Table 1). According to this analysis, a 6% error in WV estimation translates to $\sim 0.55\%$ error in TOA radiance. On the other hand, the corresponding MODIS band (Table 1) carries more uncertainties ($\sim 0.7\%$). Similar uncertainties ($\sim 0.72\%$) were found for the corresponding OLI and MSI channels (near-nadir viewing). In the following sections, we will also analyze the utility of 2230 and 2255 nm @ $FWHM=50$ nm as alternative bands within the 2200nm window.

3. Atmospheric correction

Following the selection of alternative channels, it is desired to analyze how suitable different band combinations are for the GW94 atmospheric correction algorithm [2]. The governing equation used for the retrieval of remote sensing reflectance is given as below

$$\rho_t = \{t\rho_w\} + \{\rho_r + \rho_a + \rho_{ar}\} + \{\rho_{wc} + \rho_g\} \quad (2)$$

where t is the diffuse transmission, ρ_r is the Rayleigh reflectance in the absence of aerosol, ρ_a is the scattered reflectance arising solely from aerosols, and ρ_{ar} is the reflectance arising from Rayleigh-aerosol multiple scattering, and ρ_w is the water-leaving reflectance, which is essentially equivalent of πR_{rs} [2,4,6]. The last two components, i.e., ρ_{wc} and ρ_g , correspond to the directly transmitted whitecap reflectance and the direct sunglint reflectance [31], respectively. These two terms, however, are ignored in this study for simplicity. Also, for brevity, the spectral dependency of all the components in Eq. (2) is dropped. Briefly, the AC process begins with accounting for gaseous absorption as well as removing the contribution of Rayleigh scattering using ancillary data (e.g., surface pressure, ozone, wind speed) and look-up-tables (LUTs) given per-pixel geometry information. In this study, we assume that there are no errors associated with the gaseous and Rayleigh corrections. The algorithm then uses Rayleigh-corrected reflectance (or radiance) to estimate the dominant aerosol type and thickness using pre-defined LUTs of 10 aerosol models, each of which is given for 8 different relative humidities [32]. For each model, the epsilon (ϵ) is derived in the single scattering approximation as below

$$\epsilon(\lambda, \lambda_0) = \frac{\rho_{as}(\lambda)}{\rho_{as}(\lambda_0)} \quad (3)$$

where λ_0 is a reference wavelength (the longer wavelength used in the AC) and $\rho_{as}(\lambda)$ is the spectral single scattering (SS) aerosol reflectance obtained as follows

$$\rho_{as}(\lambda) = [\omega(\lambda)\tau(\lambda)p(\Theta, \lambda)] / (4\cos(SZA)\cos(VZA)) \quad (4)$$

where ω represents the aerosol layer single scattering albedo (SSA), τ is the aerosol optical thickness (AOT), Θ represents the scattering angle, and $p(\Theta, \lambda)$ is the phase function modulated by the surface Fresnel reflection [33].

In order to test the sensitivity of the alternative SWIR channels proposed here, the standard aerosol LUTs [32] were re-created for the alternative channels (1565, 1610, 1675, 2230, and 2255nm). To do so, the aerosol microphysical properties and size distributions for the 80 aerosol types were supplied to the Mie code to generate the optical properties, such as the extinction coefficients, single scattering albedo, phase functions, and the Legendre polynomials for all the spectral channels. These properties are derived for spectra ranging from 400nm to 2500nm. The single-scattering aerosol reflectance was then computed using Eq. (4) for a black ocean [2]. The GW94 algorithm finds the best aerosol models by transforming from multiple scattering (MS) to single scattering (SS), i.e., $\rho_t - \rho_r$ to ρ_{as} , and then converting back to the multiple scattering space. In this study, it is assumed that minimal errors are propagated in the MS-to-SS and/or the SS-to-MS conversions. Therefore, all the analyses are done in the SS approximations. The ρ_{as} calculations are performed for the following imaging geometries: $VZA = 0^\circ, 40^\circ, 60^\circ$ and $SZA = 20^\circ, 30^\circ, 40^\circ, 50^\circ, 60^\circ$. For all the simulations, the relative azimuth angle was held constant at 0° . The simulations of ρ_{as} are then spectrally resampled by 28 RSRs, which encompass all the MODIS visible, NIR, and SWIR bands, the alternative SWIR bands, as well as the SWIR bands on VIIRS, and OLI. With these simulations, we have a look-up-table of aerosols similar to [32] but given for one relative humidity (i.e., RH=80%) and different viewing geometries and spectral bands.

3.1 Aerosol test models

To evaluate the sensitivity of different band combinations to various aerosol models, 16 different aerosol models were created. Ten of the test models were generated by slightly adjusting the size distribution and/or refractive indices of the original aerosol models [32]. The adjustments made included up to 20% change in either the radii or the indices of refraction of the fine and coarse modes of the aerosol models. The adjusted microphysical properties were supplied to the Mie code to generate the corresponding optical properties. These ten models are referred to as M1 (fine-mode dominated) through M10 (coarse-mode dominated). Furthermore, we defined six other test aerosol models (i.e., M11 through M16) derived from historic observations at coastal AERONET sites [34]. These sites include Helgoland (The Netherlands), LISCO (New York, USA), Oostende (Belgium), Venise (Italy), Villefranche (southern France), Wave_CIS (Louisiana, USA). To determine the microphysical properties, the slightly modified methodology proposed in [35] was used, i.e., the parameterization of the microphysical properties are improved by adding the angstrom exponent in the retrieval process. The size distribution parameters (given in the volume space) and indices of refraction for these sites are tabulated in Table 2. The real and imaginary parts of the aerosols are representative of the 869nm channel. The corresponding SSA spectra for these models are given in Appendix. These test models were supplied to Eq. (4) to simulate ρ_{as} for the imaging geometries indicated above. The AOT(869) was allowed to vary from 0.02 to 0.3 (i.e., 10 cases). The epsilon values, i.e., $\varepsilon(\lambda, \lambda_0)$, for different band combinations were then used as inputs to the aerosol correction procedure [2] to retrieve ρ_w (443). Note that the retrievals are done for a black ocean, thus, ρ_w (443) is known to be zero. In other words, we assess the retrievals by comparing estimated aerosol reflectance ($\tilde{\rho}_{as}$) and the input test aerosol model (ρ_{as}^i). The choice of the ρ_w does not impact the comparisons made throughout this manuscript.

Table 2. The size distribution and microphysical properties of the AERONET-derived test models.

Site	r_{vf}	σ_f	r_{vc}	σ_v	$\%C_{vf}$	$\%C_{vc}$	$n_r(869)$	$n_i(869)$
Helgoland (M11)	0.1	0.431	2.762	0.644	0.822	0.176	1.395	6.10E-03
LISCO (M12)	0.161	0.406	3.060	0.680	0.765	0.233	1.390	5.74E-03
Oostende (M13)	0.185	0.412	3.024	0.655	0.713	0.260	1.391	5.01E-03
Venise (M14)	0.175	0.431	2.934	0.654	0.740	0.268	1.411	7.08E-03
Villefranche (M15)	0.170	0.420	2.887	0.671	0.739	0.271	1.383	8.10E-03
Wave-CIS (M16)	0.159	0.438	2.586	0.669	0.372	0.610	1.395	4.15E-03

The analyses are carried out for all the AOTs and band combinations to encompass all possible conditions. Note that all the tests are carried out for the 80% humidity. The absolute percentage difference (APD) was used to gauge the performance:

$$APD^i(\lambda = 443\text{nm}, VZA, SZA, AOT) = \left| \rho_{as}^i - \tilde{\rho}_{as} \right| / \rho_{as}^i \times 100 \quad (5)$$

Alternatively, the difference in ρ_{as}^i and $\tilde{\rho}_{asas}$ ($\delta\rho$) is also analyzed.

3.2 Results

The sensitivity analyses were conducted for 17 different combinations of NIR and SWIR bands shown on the x-axis of Fig. 4. The band combinations were selected to synthesize the performance of the channels aboard existing polar orbiting missions and to demonstrate the performance of alternative SWIR channels within the 1600 and 2200nm windows. Figure 4 shows the median APD (upper panel) associated with the retrievals for models 1 through 8, i.e., excluding purely oceanic aerosols, which are variations of existing models [32]. The % retrievals (lower panel) are defined as

$$\% \text{Retrievals} = n[APD^{<5\%}] / N \times 100 \quad (6)$$

where $n[APD^{<5\%}]$ indicates the number of cases with errors $< 5\%$ and N is the total number of cases considered. These basic statistics are computed for $AOT(869) < 0.3$ and sun-sensor geometries ($N = 751$). Note that the performance is evaluated for $(\rho_w(443) = 0)$. The APD ranges from 5% to 20% with the 748/869 band pair exhibiting the lowest median APD. It is evident that the combination of alternative 1600nm channels (shown in red), i.e., 1565/1610, 1565/1675, and 1610/1675, performs equally well (or better) than other band combinations. The 1565/1675 and 1240/2130 band pairs, for instance, show very similar ($\sim 12\%$) errors. This is also evident from % retrievals (lower panel) where the alternative bands are found more

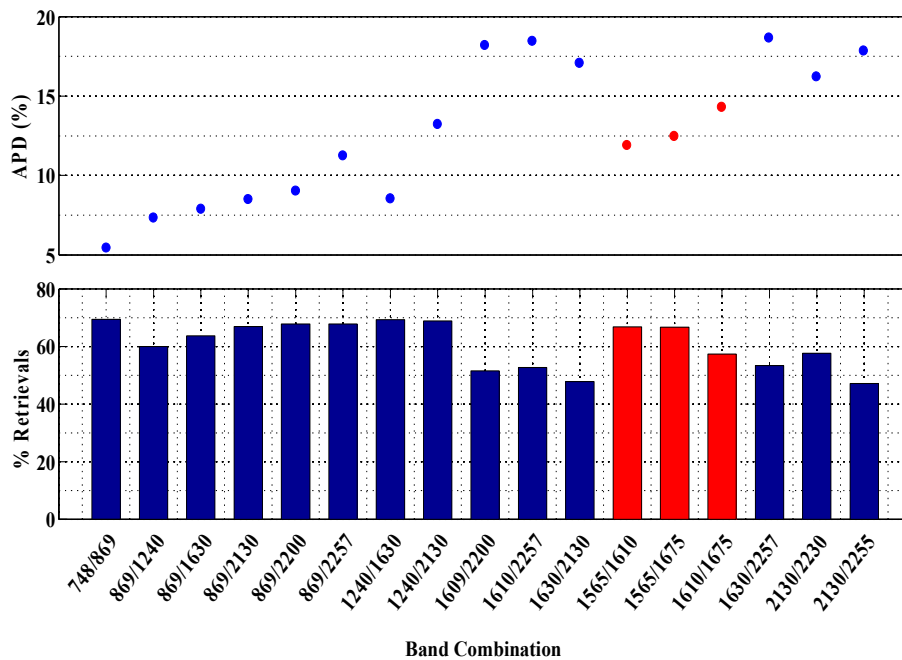


Fig. 4. The median absolute percent difference (APD) and the % retrievals (lower panel) are shown for the evaluation of the performance of AC at $\rho_w(443)$ using 17 different band combinations. The performance is merely shown for models 1 through 8 (modified models in [32]). It is evident that the combinations of new channels (shown in red) are sufficiently sensitive to these aerosol models and imaging geometries.

sensitive to various imaging scenarios than that of 1610/2257 or 1609/2200 corresponding to the VIIRS (or SLSTR) and OLI (or MSI) bands, respectively. Furthermore, the 1240/1630nm and 1240/2130nm perform just slightly better than the alternative 1600nm band combinations in terms of the % retrievals. Note that if 10% error is accepted as the threshold, i.e., $APD^{<10\%}$ is used in Eq. (6), the performance of 748/869 combination reaches $> 95\%$ while most other SWIR band pairs reach $\sim 80\%$.

The performance of the AC for models 11 through 16, i.e., AERONET-derived coastal models, is shown in Fig. 5. The mean statistics are derived from 967 different simulations with $AOT(869) < 0.3$. Comparing to Fig. 4, significantly larger APDs and lower % retrievals are obtained. It is inferred that the combination of alternative (1600nm) bands outperforms most SWIR band combinations and performs equally as well as the 748/869 combination. The degraded retrievals (% retrievals $< 50\%$) are attributed to the fact that the existing aerosol LUT [32] does not well represent aerosol optical properties in coastal areas analyzed here (see Appendix). However, if larger errors can be tolerated, i.e., $APD^{<10\%}$ used in Eq. (6), the % retrievals can reach 80% and 72% for the 748/869 and 1565/1675 band combinations.

The above analyses are provided for the 443nm band. Similarly, we further examined the retrieval errors for the MODIS 667nm. The results (not shown here) indicated similar relative performances for all the band combinations with 748/869 and 1630/2257 exhibiting best and worst performances, respectively.

We further evaluated the performance of the AC for nine selected models and two extreme geometries with a median $AOT(869)$ of 0.1. Figure 6 illustrates the difference in magnitudes of ρ_{as} and $\tilde{\rho}_{as}$ ($\delta\rho$ in reflectance units) as a metric to gauge the performance for $SZA = 40^\circ$ and a nadir-viewing geometry. The $\delta\rho$ can readily be converted to $1/sr$ units by dividing by π . The performance is noticeably varying for different models. This implies model-dependent performance at the center of the scan.

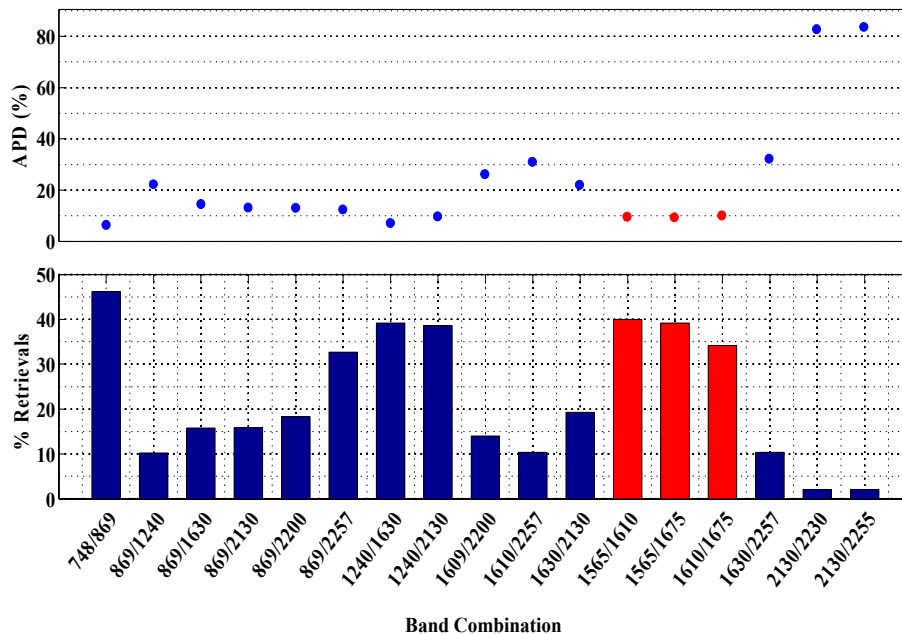


Fig. 5. The performance of AC assessed for models 11-16, i.e., AERONET-derived aerosol models. It is evident that the combinations of alternative channels (shown in red) a) perform as well as the 748/869 and b) outperform most other SWIR band combinations. It is worthwhile noting that 748/869 band pair provides most valid retrievals and the lowest mean error.

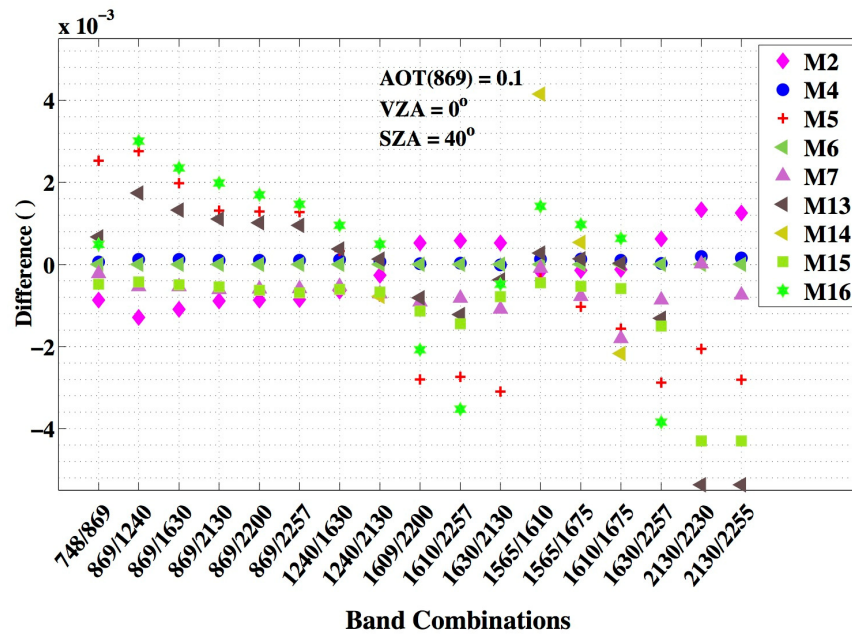


Fig. 6. The performance of the AC shown for different band combinations given for nine different aerosol test models. The difference between the retrieved aerosol reflectance and input aerosol reflectance is regarded as the error metric. The NIR band combination (i.e., 748/869nm) indicates most consistent performance across various aerosol models. The analysis is given for a median AOT(869) of 0.1 and a nadir-viewing geometry. The combination of alternative bands within the 1600nm window (e.g., 1565/1675nm) is found to lead to relatively stable errors.

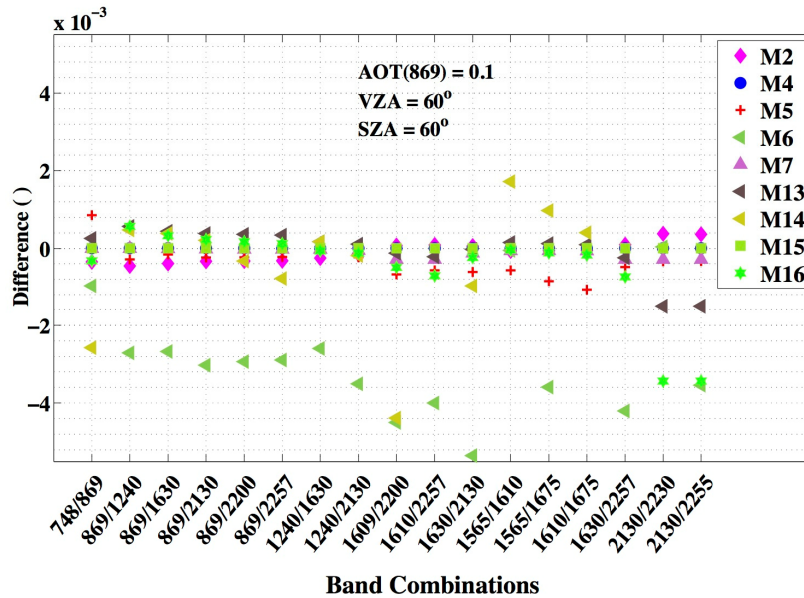


Fig. 7. The performance of the ACO shown for different band combinations given for nine different aerosol test models. The difference between the retrieved aerosol reflectance and input aerosol reflectance is regarded as the error metric. The analysis is given for a median AOT(869) of 0.1 and at VZA = SZA = 60°. The combination of alternative bands within the 1600nm window (e.g., 1565/1675nm) is found to yield satisfactory results.

It is found that the 748/869 band pair provides the most robust results (i.e., small variability) with minimal errors mostly within ± 0.001 range. Amongst all the SWIR band combinations, 1240/2130nm and 1565/1675nm are found to exhibit most consistent results. Note that most of these test models represent coastal aerosols primarily dominated with fine mode particles with very minimal absorption. The geometry examined in Fig. 6, is typical of nadir (or near-nadir) viewing satellite imagers, such as OLI and MSI. Figure 7 shows the performance of the same subset of models for large air mass fractions, i.e., $SZA = VZA = 60^\circ$. Similar to Fig. 6, the performance of the NIR band pair is amongst the most stable retrievals at this sun-viewing geometry. For instance, most of the band combinations do not perform well when M6 is examined. M6 has been modeled by adding 0.05 to the real part of the index of refraction of the original model 6. Except for M6, similar to Fig.6, the 1240/1630 and 1240/2130 combinations show the most robust performance amongst all the SWIR band combinations.

The different band combinations seem to perform more consistent given various models at large air mass fractions. To further examine the dependency on SZA, we plotted the mean retrieval errors as a function of SZA. Figure 8 illustrates the performance of different band pairs as a function of SZA. The performance is illustrated for two sets of models, i.e., M1-M7 (left) and M11-M16, given $VZA = 45^\circ$, $AOT(869) < 0.2$, and a subset of band pairs. For M1-M7 the performance tends to degrade towards larger SZAs when the SWIR bands are used. However, similar to findings in Gordon and Wang [2], no appreciable trend is found for the performance of 748/869 as a function of SZA. The combination of alternative 1600nm channels (i.e., 1565/1675) yields similar trends as for other SWIR band combinations (e.g., 1240/1630). Overall, larger errors are found for the M11-M16 (right), which were derived from historic observations at the AERONET stations (note the differences in the scales of the plots). This plot further indicates no particular trends in errors as a function of SZA for most band combinations except for the alternative bands within the 2200nm window (e.g., 2130/2257). Similar trends were found when a similar analysis was carried out for was carried out for $VZA = 0^\circ$. For this geometry and M1-M7, larger errors were found at $SZA = 30^\circ$, where the observer becomes closer to the backscattering direction.

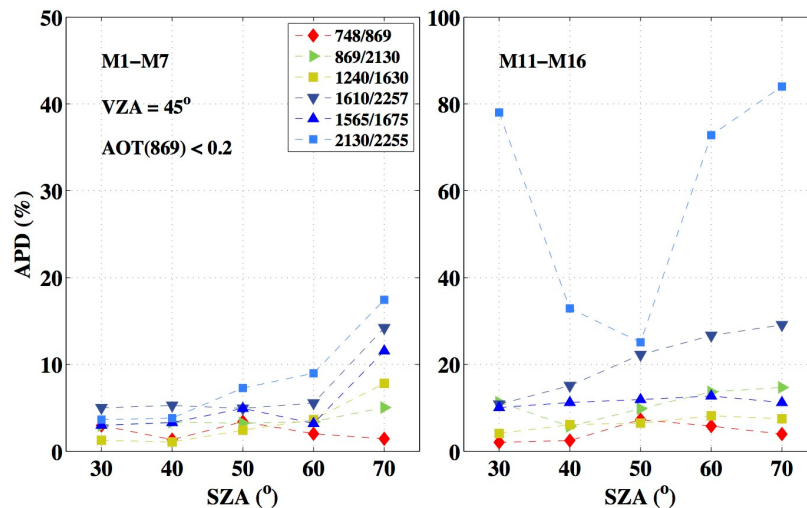


Fig. 8. The median APD (%) shown as a function of solar zenith angles (SZA) for models M1-M8 (left) and M11-M16. The median performance is found to only slightly vary for most band combinations for $30 \leq SZA \leq 60$ except that of the SWIR band pairs (i.e., 1610-2257). The performance of 748-869 is stable across the SZA range. The overall magnitude of the errors is larger for M11-M16 (AERONE-derived models derived nearby coastal areas).

For M11-M16, large errors were also found for 2130/2257 and 1610/2257 whereas 1565/1675 showed, on average, smallest errors. The model- and/or geometry-dependency of the performance of AC are thought to be attributed to the changes in the phase angle and, as a result, a change in the sensitivity of test models to the 10 aerosol models [32]. Since larger APDs are found when the test aerosol models derived from the AERONET coastal stations, it is surmised that there is a need to further expand coastal aerosol models to better represent coastal aerosols in the operational aerosol LUT.

The results presented thus far ignore any contributions from instrument calibration uncertainties or non-negligible water-leaving radiances in the NIR and SWIR regions. A series of sensitivity analyses are followed to address how these factors impact the utility of alternative SWIR bands.

4. Calibration uncertainties

High uncertainties in the absolute radiometric calibration of the NIR or SWIR bands may lead to large errors in R_{rs} retrievals. Wang and Gordon [36] asserted that errors $< 10\%$ in the NIR channels yield acceptable level of errors in $R_{rs}(443)$ for $AOT(865) < 0.2$. Franz, Bailey, Werdell, and McClain [37] also carried out a sensitivity analysis of the ACO to uncertainties in the NIR calibration by retrieving $R_{rs}(443)$ for various multiplicative gain factors (α), i.e., $\pm 4\%$. They concluded that the retrievals are insensitive to calibration uncertainties $< 4\%$ over open oceans. On the other hand, most ocean color missions (like MODIS) require $< 2\%$ uncertainty in all the reflective solar bands [38]. This uncertainty requirement is measured and characterized during pre-launch testing and calibration. However, the knowledge of the absolute calibration of these bands is not rigorously monitored at low signal levels.

In this section, we will revisit these analyses for coastal aerosols (with dominant fine-mode particles) for all of the NIR and NIR-SWIR band combinations and various AOTs. It is also assumed that $\rho_w(443) = 0$. The sensitivity analysis is performed by introducing up to $\pm 7\%$ errors in the NIR and/or SWIR bands for a subset of simulated spectra outlined in Section 3. These synthesized errors were applied to the two bands as multiplicative factors, i.e., $0.93 < \alpha_1 < 1.07$ and $0.93 < \alpha_2 < 1.07$. The increments were set at 0.5%, which yielded 841 combinations of calibration errors. The simulated errors were further partitioned into two groups: a) correlated and b) uncorrelated (or negatively correlated) errors. For the correlated errors, we only analyzed the retrievals errors associated with $\alpha_1 < 1.0$ or $\alpha_2 < 1.0$ and $\alpha_1 > 1.0$ or $\alpha_2 > 1.0$. In other words, the calibration offsets were assumed to either increase or decrease the aerosol reflectance. For the uncorrelated case, the errors were assumed to affect the magnitude of input signal in two different directions, i.e., $\alpha_1 < 1.0$ or $\alpha_2 > 1.0$ and $\alpha_1 > 1.0$ or $\alpha_2 < 1.0$. The total calibration for each instance of simulation is calculated as $\alpha = (\alpha_1^2 + \alpha_2^2)^{\frac{1}{2}}$. The total errors ranging from 0.005 to 0.07 were binned into $\Delta \sim 0.013$ ($\alpha = 1.3\%$) intervals. The APD is calculated similar to Eq. (5) as below:

$$APD^i(\lambda = 443\text{nm}, VZA, SZA, AOT) = \left| \rho_{as}^{i, \alpha_{1,2}} - \rho_{as}^{\alpha_{1,2}=1} \right| / \rho_{as}^{\alpha_{1,2}=1} \times 100 \quad (7)$$

where $\rho_{as}^{i, \alpha_{1,2}}$ is an instance of $\rho_{as}(443)$ retrieval (i) derived from two NIR and/or SWIR bands scaled by α_1 and α_2 whereas $\rho_{as}^{\alpha_{1,2}=1}$ represents the retrievals at 443nm from an unperturbed spectrum (for which unity gains were applied). The median APD within each bin (Δ) is then computed to represent the total error associated with the corresponding median calibration error (α). The simulation results expressed in terms of the median APD associated with the

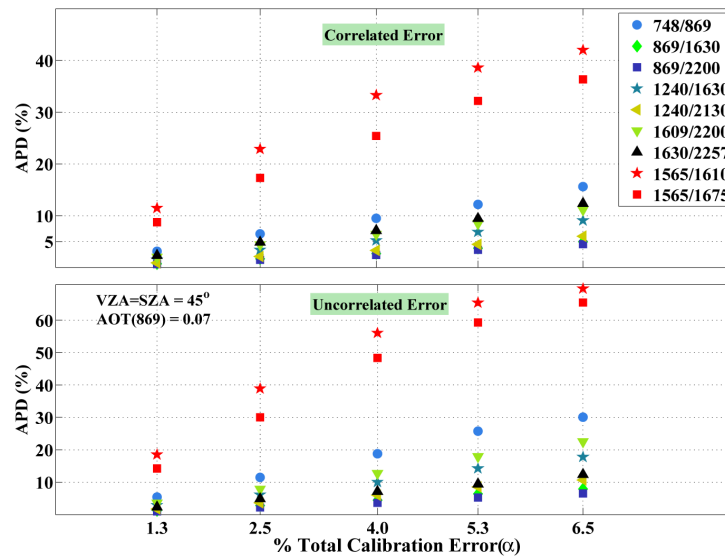


Fig. 9. The sensitivity of the AC to various calibration uncertainties for seven example band combinations given at $R_{rs}(443)$. The sensitivity, in general, increases with the band spacing of the band pairs. The combination of the new channels (i.e., 1600nm) shows the largest sensitivity to calibration uncertainties. A 0.5% uncertainty requirement is needed to ensure reasonable performance of AC using the new SWIR channels.

For M11-M16, large errors were also found for 2130/2257 and 1610/2257 whereas 1565/1675 showed, on average, smallest errors. It is inferred that the band combinations with larger intervals in the spectral space exhibit less sensitivity to calibration uncertainties. This denotes smaller uncertainties for band combinations where a NIR and a SWIR band are utilized. In addition, larger sensitivities are found when the calibration errors are uncorrelated, i.e., 50-300% larger errors depending on the absolute calibration error. The impact is, in particular, significant for band combinations with spacing $< 150\text{nm}$ (e.g., 748/869, 1565/1675). For successful retrievals using the alternative bands (1565/1675), it is vital to ensure that the total calibration errors be correlated and remain $< 1\%$. This is evident from Fig. 9. Furthermore, the heritage NIR band combination (748/869) was found very sensitive to uncorrelated calibration errors resulting in errors $> 20\%$ for $\alpha = 4\%$. The NIR-SWIR band combinations, including 869/1630 and 869/2200, are found equally insensitive to correlated errors $< 6.5\%$. Nevertheless, 869/2200 marginally outperforms the 869/1630 by only 1% for $\alpha < 6.5\%$. Both band combinations yield $\Delta\rho_w(443) < 5\%$ for $\alpha < 6\%$. These NIR-SWIR combinations have been demonstrated to perform well for retrievals from OLI data [24]. Also due to the larger spectral spacing, 1240/2130 performs better than 1240/1630 for both correlated and uncorrelated calibration errors. The band combinations of 1609/2200 and 1630/2257 are also found nearly equally sensitive to correlated calibration errors $> 4\%$, although the former is found more sensitive to uncorrelated bands. These observations will have implications for the retrievals of R_{rs} from OLI and MSI imagery using these band combinations.

Clearly, these simulations do not represent real-world imaging conditions with molecular-aerosol interactions, multiple scattering, and non-zero water-leaving radiances. Therefore, we further processed > 250 VIIRS scenes (all acquired in 2016) to synthesize calibration uncertainties and investigate the corresponding impacts on the R_{rs} products. These scenes were locally (i.e., $3 \times 3 \text{ km}^2$) processed at the locations for which aerosol optical properties were derived, i.e., LISCO, Oostende, Villefranche. We also added Lake Tahoe to include observed radiances over inland waters. These image subsets were processed to R_{rs} using the

SeaWiFS Data Analysis System (SeaDAS) by introducing calibration uncertainties to the NIR and SWIR bands (see the legend in Fig. 10). The median values computed over 5×5 - element windows were utilized to represent retrieved R_{rs} . The calibration uncertainties were modeled by scaling the (NIR or SWIR) TOA observations within the range of $\pm 10\%$ with 2% increments to reduce the computational burden. This resulted in 120 permutations in addition to the reference (“error-free”) retrieval ($R_{rs}^{\alpha_{1,2}=1}$) for which unity gains were applied to the TOA measurements. The errors in R_{rs} as a function of correlated calibration errors are illustrated in Fig. 10 in both APD (%) and RMSE (1/sr) domains. The RMSE per band combination and error interval (Δ), is computed as below

$$RMSE_{\Delta}(\lambda = 443nm) = \left[\sum_{j=1}^{j=M} \sum_{i=1}^{i=N} \left(R_{rs}^{i,\alpha_{1,2}} - R_{rs}^{j,\alpha_{1,2}=1} \right)^2 / N \times M \right]^{\frac{1}{2}} \quad (8)$$

where N is the number of instances of calibration errors falling within Δ and M is the total number of valid VIIRS subset scenes. The median VZA, SZA, and AOT(862) are also provided.

To ensure consistency with the results illustrated in Fig. 9, linear regressions (e.g., RMSE Vs. α) were performed to provide sensitivities for calibration errors given on the abscissa of Fig. 9. The upper panel (Fig. 10) clearly indicates that the results (image-based analysis) are in agreement with those shown in Fig. 9. There is, however, slightly higher sensitivity ($\sim 3\%$) to calibration errors across the range of errors. This is potentially attributed to the fact that the simulated retrievals (Fig. 9) were carried out in the single-scattering domain.

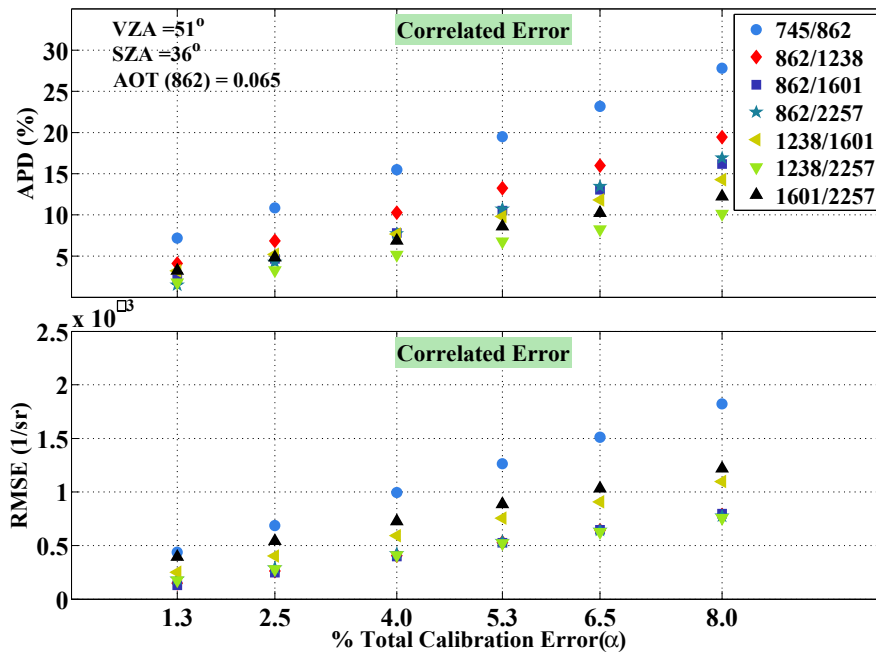


Fig. 10. The calibration sensitivity analysis obtained by simulating correlated calibration errors for the NIR and SWIR bands of VIIRS reported for $R_{rs}(443)$. The errors are given for APD (upper) and RMSE. These results are consistent with those illustrated in Fig. 9. The results indicate that the R_{rs} retrievals using 745/862 bands are sensitive to the total calibration offsets $> 1\%$.

The APDs are influenced by the magnitude of the $R_{rs}(443)$, thus, the RMSEs are also provided. The RMSEs also allow for comparisons with previous studies [36,37] that reported the errors in absolute units. It should be noted that previous studies were mostly concerned with data simulations and/or analyses for limited case scenarios over open oceans. The RMSE plot further indicates that the 1601/2257 and 1238/1601 band combinations are the second and third most sensitive combinations to calibration uncertainties. Note that the corresponding errors in R_{rs} induced by uncorrelated errors (not shown here) were found, on average, twice larger than those shown in the upper panel in Fig. 10.

5. None-zero water-leaving radiances

The simulations presented to this point assumed negligible water-leaving radiance (i.e., $\rho_w = 0$) within the NIR and SWIR portions of the spectrum. However, in extremely turbid coastal/inland waters, non-negligible water-leaving radiance is expected. In this section, we evaluate the performance of AC in the presence of non-zero water-leaving radiances within the NIR and SWIR channels. It has been asserted that there is non-negligible water-leaving radiances within the 1020nm and 1240nm SWIR windows [18,39], however, due to the lack of high-fidelity in situ instrumentation, R_{rs} spectra within the 1600nm and 2200nm windows have not been well studied. Fig. 11 illustrates a single OLI scene acquired on 12/01/2016 and processed using SeaDAS over the Arabian Sea and the Gulf of Cambay concentrations of total suspended solids are generally larger than 10 g/m^3 [40]. The R_{rs} given for 865 and 1609nm bands clearly indicate non-zero water-leaving radiances in the NIR and SWIR bands.

For this study, to find out reasonable estimates of R_{rs} within the NIR and SWIR bands, > 30 OLI scenes over extremely turbid waters were processed to R_{rs} products to derive $R_{rs}(865)$, $R_{rs}(1609)$, and $R_{rs}(2200)$. These scenes represent turbid waters in the Bay of Bangle, Yangtze River basin, the Mississippi River Delta, and the Amazon River Basin. These products were obtained by the atmospheric correction carried out in SeaDAS [23] using different band combinations of the three available channels, i.e., 865/1609, 865/2200, and 865/1609. Following the AC, basic statistics, including median, mean, and standard deviations were extracted over highly turbid waters (i.e., nominal Chla > 5 g/m^3) from the OLI products to simulate various turbid water-leaving reflectances. It should be noted that, in this sensitivity analysis, the accuracy/precision of the R_{rs} retrievals within the NIR-SWIR region is not critical.

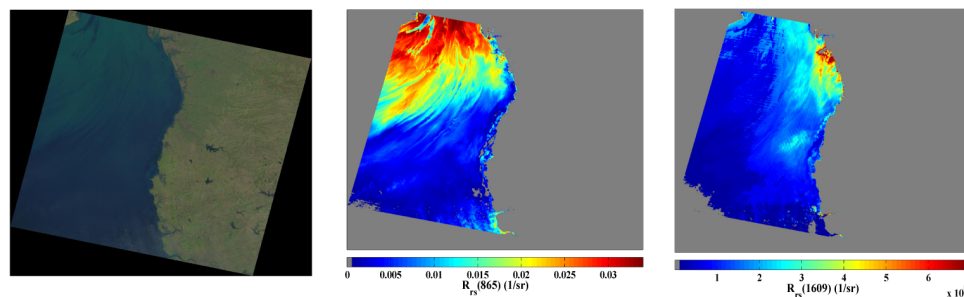


Fig. 11. The Landsat-8 OLI natural color image is shown alongside the remote-sensing reflectance products derived for the 865 and 1609nm bands. Significant backscattered signals and high (qualitative) correlation between $R_{rs}(865)$ and $R_{rs}(1609)$ are evident from the spatial patterns. The image was collected on January 12th 2016.

A linear interpolation/extrapolation was further carried out to estimate R_{rs} for other channels examined in this study, i.e., $865\text{nm} \leq \lambda \leq 2257\text{nm}$. Recognizing the high backscattered signal at 748 nm, we excluded this channel in the analysis. The combination of

various R_{rs} values yielded 27 virtual multispectral R_{rs} curves three of which are tabulated in Table 3. The $R_{rs}(865)$ values used here are consistent with the lower bound of values published in [41] wherein R_{rs} spectra over the sediment-dominated Yangtze River estuary are illustrated. These quantities were transmitted to top of the aerosol layer (2km) and added to the test aerosol models (Eq. (2)). The retrievals were then conducted using these spectra as input. The performance was then evaluated as below

$$APD^i(\lambda = 443nm, VZA, SZA, AOT) = \left| \rho_{as}^{i, R_{rs} \neq 0} - \rho_{as}^{R_{rs} = 0} \right| / \rho_{as}^{R_{rs} = 0} \times 100 \quad (9)$$

where $\rho_{as}^{R_{rs} = 0}$ represents retrievals assuming $R_{rs}(\lambda \geq 865nm) = 0$ whereas $\rho_{as}^{i, R_{rs} \neq 0}$ is an instance of retrieval (i) with $R_{rs}(\lambda \geq 865nm) \neq 0$. Note that similar to the previous sections $\rho_w(443) = 0$.

Table 3. Three sample R_{rs} (1/ sr) spectra utilized to model extremely turbid waters

	$R_{rs}(865)$			$R_{rs}(2130)$
Case 1	0.00402	0.00168	0.000438	6.925e-05
Case 2	0.00499	0.00199	0.00043	2.871e-05
Case 3	0.00701	0.00257	0.000437	6.878e-05

The performance of the AC using different band combinations is shown in Fig. 12 (similar to Fig. 4). The performance is evaluated for a subset of test cases (~1200), which encompass various imaging geometries and $AOT(869) < 0.3$. It is important to note that comparing to Fig. 4, larger retrieval errors ranging from 25% to 45% are found. It is, thus, recognized that the performance of the AC significantly degrades over extremely turbid waters even when SWIR bands > 1560nm are utilized for the aerosol removal.

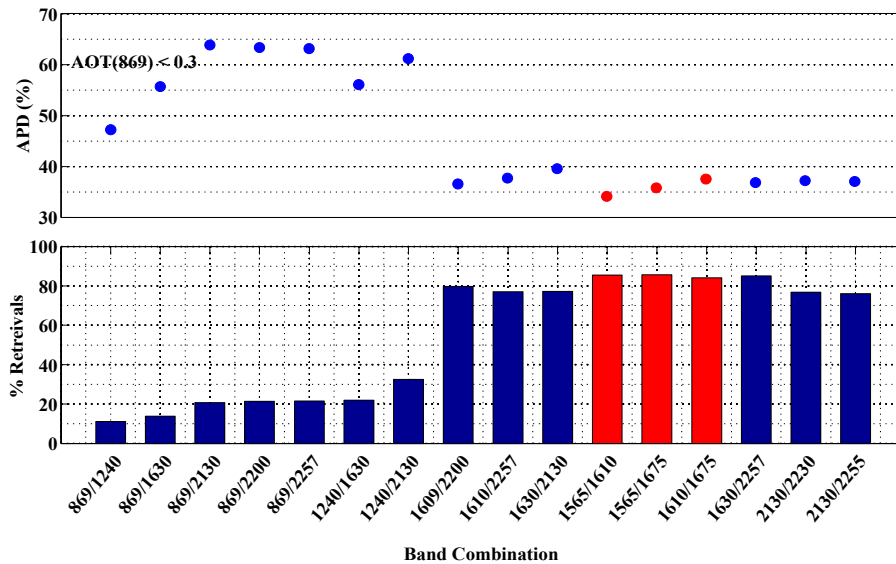


Fig. 12. The median absolute percent difference (APD) and the % retrievals (lower panel) are shown for the evaluation of the performance of the atmospheric correction (ACO) over extremely turbid waters (Table 3). It is evident that the combinations of new channels (shown in red) result in similar retrieval errors as those from existing SWIR bands combinations. Note the large errors associated with NIR-SWIR band combinations. No attempt for the removal water-leaving radiance in the NIR has been made here [13].

The APDs, however, are lower when any combinations of SWIR bands $> 1560\text{nm}$ are utilized. Although the 869/1240 band combination exhibits lower APDs than those from 1240/1630, 860/2130, or 869/2257, its % retrievals (lower panel) are very low. The % retrieval is defined in Eq. (6). The highest % retrievals ($\sim 80\%$) are associated with retrievals when the alternative SWIR bands (shown in red bars) are applied.

The failure in the retrievals occurs when the computed epsilon (Eq. (3)) falls outside the range of the modeled epsilon values. The better performance of these alternative SWIR channels is also inferred from their lower APD (upper panel). Since the backscatter signal within the SWIR regions is governed primarily by the pure water absorption spectrum [17], the closer the spacing of the SWIR bands the more similar the in-water backscattered signals are. Therefore, the impact on the epsilon is minimal when removing aerosol radiance. This impact, however, is not very significant when compared to the errors in other SWIR band combinations (e.g., 1609/2200, 1630/2257). One should note that, in this study, we did not attempt to account for the non-zero water-leaving radiance associated with the NIR or SWIR bands [13,14]. The incorporation of such methods will potentially reduce the magnitude of the errors shown in Fig. 12.

6. Discussions

When designing an ocean color imager, there is always an optimal design where a balance amongst desirable science outputs, engineering challenges, and cost is met. For future OC missions when/if the latter two parameters restrict spectral radiometric observations to a range $< 1700\text{nm}$, this study has demonstrated that it is possible to utilize alternative bands at the two ends of the 1600nm window, i.e., 1565/1675, to remove/minimize aerosol contributions (assuming the GW94 algorithm is utilized). This combination is as equally sensitive to different aerosol types as the other existing band combinations and is expected to yield R_{rs} spectra in extremely turbid waters as precise as those obtained via the other SWIR band combinations. However, for a robust AC using the GW94 method, strict calibration requirements, i.e., $< 1\%$, must be met. Uncorrelated calibration uncertainties (e.g., one band biased low and one biased high) must be avoided. These two bands are further required to be sufficiently narrow, i.e., $\text{FWHM}=20\text{ nm}$, to avoid significant contaminations due to water vapor absorptions. Therefore, to maintain high SNR, the use of these bands may be limited to ocean color instruments onboard geostationary platforms.

Although this study has primarily focused on simulating retrievals of R_{rs} in coastal areas using alternative and exiting SWIR bands, the results of the calibration analysis also have implications for the retrievals using the heritage NIR band combinations in open oceans. The uncorrelated calibration offsets will also impact NIR-SWIR and SWIR-only approaches. Therefore, for the existing missions (e.g., MODIS, VIIRS, OLI, MSI, and SLSTR) and multi-mission product merging practices, it is vital to ensure that the calibrations of these bands are well-characterized post-launch using either vicarious or cross-calibration approaches over open ocean areas. This is to determine any potential correlated/uncorrelated calibration offsets in the NIR and SWIR bands. In particular, for coastal-dominated aerosol conditions, the atmospheric correction using the NIR bands (e.g., 748/869) was found sensitive to calibration uncertainties. The calibration analyses carried out in this study were different from the previous studies [36,37] wherein calibration offsets of the NIR bands were examined for a limited set of simulations and/or analyses. It should be emphasized that this study assumed no errors in a) the removal of Rayleigh contributions and b) the single-scattering to multiple-scattering conversion (or vice versa). Any additional errors due to these processes could either exacerbate or enhance the results presented here. In addition, efforts must be made to characterize and minimize uncorrelated (or negatively correlated) calibration errors, which can lead to significant uncertainties in R_{rs} retrievals. According to the results in Section 5, it is expected that the errors in the non-zero water-leaving radiances in the NIR and SWIR dominate the total error budget (i.e., there less sensitivity to the choice of aerosol models),

which highlights the need for the removal of water-leaving radiances using appropriate bio-optical models.

7. Conclusion

The addition of the SWIR bands onboard ocean color mission requires a strong justification as adding such capabilities bears significant cost and engineering challenges. This manuscript seeks to evaluate the usability of alternative SWIR bands within the 1600nm window to allow for the exclusion of bands within the 2200nm window onboard geostationary missions. We examined the band-ratio based atmospheric correction [2] using alternative SWIR bands and compared the results with those from the existing NIR-SWIR bands onboard existing polar orbiting missions. It was found that the two alternative narrow bands, i.e., 1565/1675, provide sufficient sensitivity to various aerosol models. The two bands were also found to yield reasonable retrievals in extreme water turbidity levels. Nevertheless, for successful retrievals of water-leaving reflectance ($\Delta\rho_w < 5\%$) the total uncertainty budget for the calibration of these alternative SWIR bands must be better than 1%. Overall, the sensitivity to calibration uncertainties is expected to be high for closely spaced (i.e., $< 150\text{nm}$) spectral bands. Therefore, it is possible to successfully process ocean color products over coastal waters using these SWIR channels provided they are well characterized and calibrated. When using the existing SWIR bands (e.g., OLI, MSI, or VIIRS) for atmospheric correction, care must be taken regarding the interpretation of the results as small calibration errors can induce high uncertainties in R_{rs} products. Future studies may be dedicated to demonstrating these analyses using recorded coastal imagery, including hyperspectral airborne images, in coastal/inland waters.

Appendix

The optical properties of the aerosol test models derived from AERONET stations, including Helgoland (M10), LISCO (M11), Oostende (M12), Venise (M13), Villefranche (M14), and Wave_CIS (M15), were computed using the Mie theory. The corresponding spectra of single scattering albedo (SSA) are compared against the modified standard models (M1-M7) in Fig. 13.

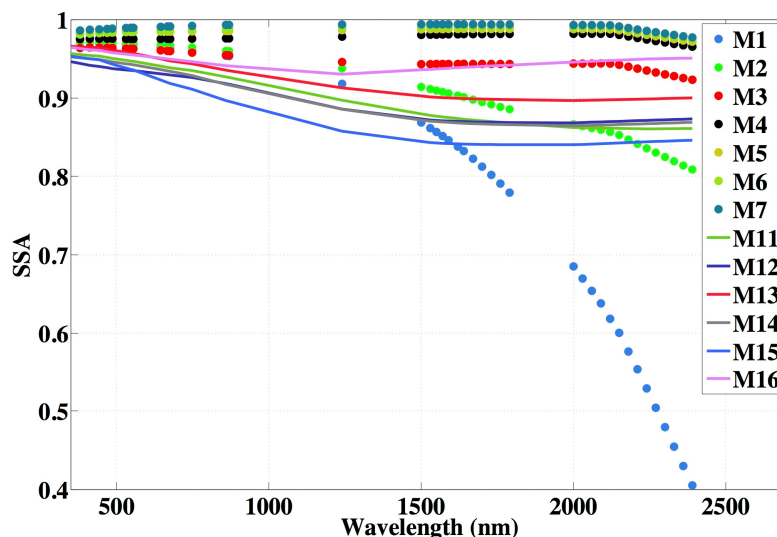


Fig. 13. The SSA spectra shown for various aerosol models. M1-M7 are the modified standard models used for AC in operational processing and M11-M16 are those derived from six AERONET stations.

Both shapes and magnitudes of M11-M16 noticeably differ from those of M1-M7 suggesting that relatively large errors in the retrievals of Rrs may be expected at these coastal stations. Note that the coastal models represented in [32] were derived from three AERONET sites in Chesapeake Bay region. The median AOT at 550nm for these sites were 0.152, 0.127, 0.175, 0.235, 0.168, and 0.138, respectively and the median angstrom exponents calculated from the 440-870nm bands were 1.0, 1.68, 1.13, 1.45, 1.36, and 1.19, respectively.

Acknowledgment

We greatly appreciate Bryan Franz with the Ocean Ecology Laboratory (OEL) at NASA Goddard Space Flight Center (GSFC) for his insights and comments that improved the presentation of this manuscript. The primary funding support for this study was granted by the NASA Headquarters as part of the Geo-CAPE mission pre-formulation studies. We also thank Brian Cairns with the Goddard Institute for Space Studies for a fruitful discussion on the absorption of the well-mixed gases.